

RESEARCH ARTICLE

10.1002/2016JA023831

Special Section:

Magnetospheric Multiscale (MMS) mission results throughout the first primary mission phase

Key Points:

- PIC simulations of asymmetric magnetic reconnection including both hot and cold magnetospheric ion populations
- Cold ions sustain electromagnetic structures at scales lower than the hot ion Larmor radius in magnetic reconnection
- Explanation of the mechanism leading to an extended Larmor electric field region in the presence of cold ions

Correspondence to:

J. Dargent,
jeremy.dargent@lpp.polytechnique.fr

Citation:

Dargent, J., N. Aunai, B. Lavraud, S. Toledo-Redondo, M. A. Shay, P. A. Cassak, and K. Malakit (2017), Kinetic simulation of asymmetric magnetic reconnection with cold ions, *J. Geophys. Res. Space Physics*, 122, 5290–5306, doi:10.1002/2016JA023831.

Received 21 DEC 2016

Accepted 24 APR 2017

Accepted article online 10 MAY 2017

Published online 22 MAY 2017

Kinetic simulation of asymmetric magnetic reconnection with cold ions

J. Dargent^{1,2,3} , N. Aunai¹ , B. Lavraud^{2,3} , S. Toledo-Redondo⁴ , M. A. Shay⁵ , P. A. Cassak⁶ , and K. Malakit⁷ 

¹LPP, CNRS, Ecole polytechnique, UPMC Univ Paris 06, University Paris-Sud, Observatoire de Paris, University Paris-Saclay, Sorbonne Universités, PSL Research University, Palaiseau, France, ²Institut de Recherche en Astrophysique et Planétologie, Université de Toulouse, Toulouse, France, ³Centre National de la Recherche Scientifique, Toulouse, France, ⁴Science Directorate, European Space Agency, ESAC, Madrid, Spain, ⁵Bartol Research Institute, Department of Physics and Astronomy, University of Delaware, Newark, Delaware, USA, ⁶Department of Physics and Astronomy, West Virginia University, Morgantown, West Virginia, USA, ⁷Department of Physics, Faculty of Science and Technology, Thammasat University, Pathum Thani, Thailand

Abstract At the dayside magnetopause, the magnetosphere often contains a cold ion population of ionospheric origin. This population is not always detectable by particle instruments due to its low energy, despite having an important contribution to the total ion density and therefore an impact on key plasma processes such as magnetic reconnection. The exact role and implications of this low-temperature population are still not well known and has not been addressed with numerical simulation before. We present 2-D fully kinetic simulations of asymmetric magnetic reconnection with and without a cold ion population on the magnetospheric side of the magnetopause, but sharing the same total density, temperature, and magnetic field profiles. The comparison of the simulations suggests that cold ions directly impact signatures recently suggested as a good marker of the X line region: the Larmor electric field. Our simulations reveal that this electric field, initially present all along the magnetospheric separatrix, is related to the bounce of magnetosheath ions at the magnetopause magnetic field reversal through Speiser-like orbits. Once reconnection widens the current sheet away from the X line, the bouncing stops and the electric field signature remains solely confined near the X line. When cold ions are present, however, their very low temperature enables them to $\mathbf{E} \times \mathbf{B}$ drift in the electric field structure. If their density is large enough compared to other ions, their contribution to the momentum equation is capable of maintaining the signature away from the X line. This effect must be taken into account when analyzing in situ spacecraft measurements.

1. Introduction

Magnetic reconnection at the Earth's dayside magnetopause involves ion populations from both the magnetosheath and the magnetosphere. These populations greatly differ, leading to asymmetric boundary conditions. The magnetosheath plasma is typically denser than the magnetosphere (e.g., $n \sim 10 \text{ cm}^{-3}$ versus 0.5 cm^{-3}) and the magnetic field weaker (e.g., $B \sim 40 \text{ nT}$ versus 60 nT) [Baumjohann and Treumann, 1997; De Keyser et al., 2005]. This asymmetry produces typical magnetic reconnection signatures, such as a possible shift of the X line on the magnetospheric side and a wider exhaust on magnetosheath side [De Keyser et al., 2005; Cassak and Shay, 2007; Pritchett, 2008]. The Hall electric field, which results from decoupling between demagnetized ions and frozen-in electrons, is strongly asymmetric. It mostly develops on the magnetospheric side and points outward [Mozer et al., 2008]. Another such signature is the so-called Larmor electric field [Malakit et al., 2013], located near the X line, normal to the current sheet and which sign is the inverse of the Hall electric field. All those signatures are affected by the properties of the upstream plasmas.

The magnetosphere is usually not composed of only one population but often involves several with quite distinct characteristics. In particular, near the dayside magnetopause, a low-energy population, hereafter referred to cold ions, is often observed [Sauvaud et al., 2001; André and Cully, 2012; Walsh et al., 2014; Fuselier et al., 2016]. These ions have energies in the range 0–100 eV, to be compared with hotter ions of plasma sheet origin at several keV to tens of keV [Sauvaud et al., 2001; Toledo-Redondo et al., 2015]. Due to their low energy, cold ions are often at the limit of detection for spacecraft particle instruments [Sauvaud et al., 2001;

André and Cully, 2012]. This cold population comes from the ionosphere by various means [*André and Cully, 2012; Fuselier et al., 2016*]. The polar wind, or warm plasma cloak, is an outflow of cold ions through the polar cusp, where magnetic field lines are open. It escapes from the ionosphere and reaches the magnetopause, mainly on the nightside in the magnetotail, and also on the dayside to the magnetopause. These cold ions mainly affect high latitudes, but we also observe an outflow at lower latitudes, called plasmaspheric wind [*Matsui et al., 1999*], bringing cold ions to the magnetopause $\sim 70\%$ of the time [*André and Cully, 2012*]. This outflow has a density of $0.5\text{--}3\text{ cm}^{-3}$, which is of the same order or larger than the density of hot ions. Another origin for cold ions is the plasmaspheric plumes. Resulting from a change in the convection properties in the inner magnetosphere, they form a tongue of very dense and low-energy plasma eventually reaching the magnetopause. Plumes are not as frequent as the other outflows ($\sim 20\%$ of the time), but they bring a very large amount of plasma ($3\text{--}40\text{ cm}^{-3}$) [*Borovsky and Denton, 2006; Borovsky et al., 2008*]. During plasmaspheric plume events, we observe a mass loading of the upstream plasma at the magnetopause, impacting the reconnection rate [*Borovsky and Denton, 2006; Borovsky et al., 2008; Walsh et al., 2014; Wang et al., 2015*]. Together with the plasmaspheric wind, these populations of cold ions represent an important contribution to the total particle density, especially in the equatorial plane where magnetic reconnection and the Magnetospheric Multiscale (MMS) spacecraft operate [*Burch et al., 2016*].

If the impact of the cold ion density on magnetic reconnection, i.e., mass loading, has been studied [*Borovsky et al., 2008; Walsh et al., 2014*], much less is known about the effect associated with their very low temperature. Because the environment is collisionless, plasma populations with very different energies can coexist and have various effects on magnetic reconnection. For example, the presence of both hot and cold magnetospheric ions results in intrinsic reconnection scales associated with both hot and cold ions [*André et al., 2010; Toledo-Redondo et al., 2015; Toledo-Redondo et al., 2016a*]. From the kinetic viewpoint, their very different temperatures result in distinct particle dynamics, with the existence of a region where hot ions are demagnetized while cold ions are not [*André et al., 2010; Lee et al., 2014; Toledo-Redondo et al., 2016a*]. Until now, our knowledge on cold ion dynamics and their role in magnetopause reconnection has been mainly addressed using spacecraft observations [*Lee et al., 2014; Wang et al., 2015; Toledo-Redondo et al., 2016b*]. *Borovsky and Hesse [2007]* studied the impact of mass loading on magnetic reconnection, but they used MHD simulations and did not investigate the role of the temperature. In this paper, we use numerical simulations to provide a reproducible, simple, and complementary viewpoint on this problem. Due to the kinetic nature of the problem we use a fully kinetic particle-in-cell (PIC) code.

Using two-dimensional (2-D) fully kinetic simulations, we model asymmetric magnetic reconnection with and without cold ions. We are interested in the dynamics of these ions and the impact of having two magnetospheric ion populations with very different temperatures. In order to isolate the effects from well-known fluid behavior such as the system mass loading, we keep exactly the same macroscopic quantities for the initial condition of both simulations, so that the only difference between them is the multicomponent property of the magnetospheric ion distributions: either only one ion population or two ion populations (a hot one and a cold one). In those simulations, we observe in particular an impact of cold ions on the Larmor electric field signature.

The present paper is organized as follows. Section 2 details the data normalization used by the numerical model and the method used to introduce cold ions in the simulation. In section 3, we look at the fields near the X line in both simulations and focus on the mechanism underlying the presence of the Larmor electric field. In section 4, we look at the fields along the separatrix and far from the X line in both simulations. We explain in particular why, without cold ions, the Larmor electric field only appears near the X line, whereas with cold ions a similar field appears all along the magnetospheric separatrix. Finally, section 5 presents a summary and some outlook.

2. Setup of Simulations With and Without Cold Ions

In this paper, we present two fully kinetic simulations of asymmetric magnetic reconnection in a two-dimensional (2-D) geometry using the particle-in-cell (PIC) code SMILEI (see <http://www.maisondelasimulation.fr/smilei>). Both simulations share the same electromagnetic setup, total density, and temperature profiles. They only differ by the velocity distribution of the plasma particles. The first one is a reference simulation, with only the ion populations representing the magnetosheath on one side and the hotter magnetosphere on the

other side. The second simulation has three ion populations, a magnetosheath population on one side, as in the first run, and two populations on the magnetospheric side: a hot and a much colder one.

2.1. General Setup

The data presented are normalized using ion scale quantities. The magnetic field and density are normalized to arbitrary value B_0 and n_0 , respectively. The masses and charges are normalized to the proton mass m_p and charge e , time is normalized to the inverse of the proton gyrofrequency $\omega_{ci}^{-1} = m_p / eB_0$ and length to the proton inertial length $\delta_i = c / \omega_{pi}$, where c is the speed of light in vacuum and $\omega_{pi} = \sqrt{n_0 e^2 / m_p \epsilon_0}$ is the proton plasma frequency.

The initialization of both runs consists in two current layers in the (x, y) plane in a domain of size $(x_{\max}, y_{\max}) = (320, 128)\delta_i$. There are $n_x = 6400$ cells in the x direction, $n_y = 5120$ cells in the y direction, and initially 50 particles per cell and per population. Plasma moments and electromagnetic forces are calculated using second-order interpolation. Particles are loaded using local Maxwellian distributions. The time step is calculated using a Courant-Friedrichs-Lewy (CFL) condition leading to $dt = 8.4 \cdot 10^{-4}$ and the total simulation time is $T = 160$. The double layer configuration allows a full periodic system, i.e., periodic domain boundary conditions in both x and y directions [Drake et al., 2006]. From now on, we will only focus on one current layer and give profiles for this layer. The half box size is $(x_m, y_m) = (320, 64)\delta_i$, with the layer located at $y_0 = y_m/2$.

To initialize both simulations, we chose an electric field \mathbf{E} null everywhere and an asymmetric antiparallel magnetic field \mathbf{B} which is along the x axis:

$$\mathbf{B}(x, y) = \frac{1}{B_r} \left[-\tanh\left(\frac{y-y_0}{L} + \arctan h\left(\frac{B_r-1}{B_r+1}\right)\right) \frac{B_r+1}{2} - \frac{B_r-1}{2} \right] \mathbf{u}_x \quad (1)$$

with $B_r = |B_{\text{sheath}}/B_{\text{sphere}}|$ the magnetic field ratio between both sides of the current sheet and \mathbf{u}_x the unit vector in the x direction. In our case, we choose $B_r = 0.5$. Using the quasi-neutrality, we set the total density $n = n_i = n_e$, given by

$$n(x, y) = \frac{1}{n_r} \left[1 + \frac{n_r-1}{2} \left(\tanh\left(\frac{y-y_0}{L}\right) + 1 \right) \right] \quad (2)$$

with $n_r = n_{\text{sheath}}/n_{\text{sphere}}$ the density ratio between both sides of the current sheet. In our case, we choose $n_r = 3$.

The total temperature $T = T_i + T_e$ is determined in order to preserve the pressure balance. The electron to ion temperature ratio is constant and chosen equal to $\theta = T_e/T_i = 0.2$. We assume that the ratio of electron and ion currents is equal to $-T_e/T_i$. The mass ratio m_i/m_e is 25. We trigger magnetic reconnection thanks to a perturbation \mathbf{B}_1 on the initial magnetic field (equation (1)):

$$\mathbf{B}_1 = B_{1x}(x, y)\mathbf{u}_x + B_{1y}(x, y)\mathbf{u}_y \quad (3)$$

$$B_{1x}(x, y) = -2\delta b \frac{y-y_0}{\sigma} \exp\left(-\frac{(x-x_0)^2 + (y-y_0)^2}{\sigma^2}\right) \quad (4)$$

$$B_{1y}(x, y) = 2\delta b \frac{x-x_0}{\sigma} \exp\left(-\frac{(x-x_0)^2 + (y-y_0)^2}{\sigma^2}\right) \quad (5)$$

where $y_0 = y_m/2$, $x_0 = x_m/2$, $\delta b = 0.12$, and $\sigma = 1$. From now on, we will name the runs without and with cold ions run A and run B, respectively.

2.2. Cold Ion Setup

The run B, with cold ions, needs two populations on the magnetosphere side. Our initial condition and numerical parameters are based on spacecraft observations from Toledo-Redondo et al. [2015]. We split ions between magnetosheath ions (ish), hot magnetospheric ions (ih), and cold magnetospheric ions (ic). To keep total densities equal as equation (2), we must have $n = n_{\text{ish}} + n_{\text{ih}} + n_{\text{ic}}$. To calculate the density profile of each species, we make the assumption that each of these species have a constant temperature in the domain. We then arbitrarily fix the magnetosheath ion density profile as follows:

$$n_{\text{ish}}(x, y) = \frac{1}{2} \left[1 + \tanh\left(\frac{y-y_0}{L}\right) \right] \quad (6)$$

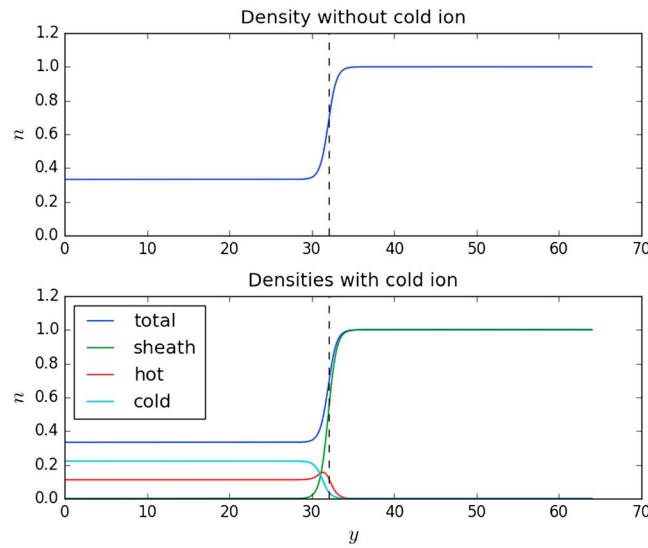


Figure 1. Initial density profile of each ion species for each run. The run A without cold ions has only one ion population. The vertical black dashed line gives the y position of the initial perturbation.

On the magnetosheath side, there is only one ion population, so equation (6) tends to the same value than equation (2), i.e., $n = 1$. On the magnetosphere side, there are two populations. We first fix their asymptotic density and temperature ratio as $n_{\text{hoc}} = n_{\text{ih}}/n_{\text{ic}} = 0.5$ and $T_{\text{hoc}} = T_{\text{ih}}/T_{\text{ic}} = 500$. Next, we use the asymptotic values of each species to determinate their temperature, which will remain the same in the whole box. The normalized pressure balance is given by this formula:

$$n_{\text{ish}} T_{\text{ish}} + n_{\text{ih}} T_{\text{ih}} + n_{\text{ic}} T_{\text{ic}} + n_e T_e + \frac{B^2}{2} = K \quad (7)$$

where K is a constant, fixed at $1/B_r^2$ in our case. On the magnetosheath side, we have $n_{\text{ish}} = n = 1$ and $n_{\text{ih}} = n_{\text{ic}} = 0$. On the magnetospheric side, we have $n_{\text{ish}} = 0$ and $n = 1/n_r = n_{\text{ih}} + n_{\text{ic}}$, so $n_{\text{ih}}/n = n_{\text{hoc}}/(1 + n_{\text{hoc}})$ and $n_{\text{ic}}/n = 1/(1 + n_{\text{hoc}})$. From those asymptotic densities and equation (7), we can deduce the temperature of each ion species:

$$T_{\text{ish}} = \frac{K - 1/2}{1 + \theta} \quad (8)$$

$$T_{\text{ic}} = \frac{n_r}{1 + \theta} \left(K - \frac{1}{2B_r^2} \right) \frac{1 + n_{\text{hoc}}}{n_{\text{hoc}} T_{\text{hoc}} + 1} \quad (9)$$

$$T_{\text{ih}} = T_{\text{ic}} T_{\text{hoc}} \quad (10)$$

With the assumption of constant temperature for each ion species, we can use these values to determine the missing density profiles. Using $n = n_{\text{ish}} + n_{\text{ih}} + n_{\text{ic}}$, we can solve equation (7) to find n_{ic} and n_{ih} everywhere:

$$n_{\text{ic}}(x, y) = \frac{T_{\text{hoc}}}{1 + T_{\text{hoc}}} \left[\frac{1}{T_{\text{ih}}} \left(\frac{K - B^2/2}{1 + \theta} - n_{\text{ish}} T_{\text{ish}} \right) + n_{\text{ish}} - n \right] \quad (11)$$

$$n_{\text{ih}}(x, y) = n - n_{\text{ish}} - n_{\text{ic}} \quad (12)$$

Electrons and electromagnetic fields are the same as in the run without cold ions. The initial density profiles of each species are shown in Figure 1.

We run both simulations until reaching a quasi steady state. They evolve in a similar way, reconnecting approximately the same amount of magnetic flux in the same time period. The reconnection rate of both simulations with and without cold ions is shown in Figure 2. From now on, we will work with data taken at $T = 120$, where the steady state of magnetic reconnection is reached for both simulations, and the reconnection rate similar.

3. Ion Kinetic Dynamics Near the X Line

The X line and its surroundings, the decoupling region, form an area where fluid assumptions are no longer satisfied. A kinetic treatment is thus necessary to fundamentally understand the mechanisms controlling reconnection and the signatures used for the detection of X line regions in spacecraft data. One of these signatures is the Larmor electric field, recently proposed from fully kinetic simulations to identify the X line region in asymmetric current sheets [Malakit et al., 2013]. This signature consists of an electric field located near the X line whose normal component points toward the magnetosphere, as opposed to the well-known strong Hall electric field, which points outward and is seen all along the magnetospheric separatrix. We will look into more details at the origin of this Larmor electric field and discuss the effect that cold ions have on it.

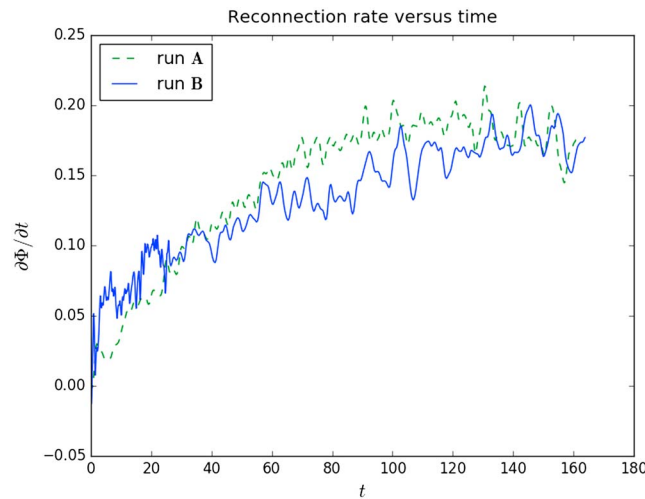


Figure 2. Reconnection rate of both simulations with (run B, thick blue curve) and without (run A, dashed green curve) cold ions. Reconnection rate is here defined as the time derivative of the magnetic flux Φ in the simulation plane (x, y) . See Shay et al. [2001] or Pritchett [2008] for a developed description of the magnetic flux and how reconnection rate comes from it.

To analyze this electric field, we start from the Ohm's law:

$$\mathbf{E} = -\mathbf{u}_i \times \mathbf{B} + \frac{1}{en} (\mathbf{j} \times \mathbf{B} - \nabla \cdot \vec{P}_e) - \frac{m_e}{e} \left(\frac{\partial \mathbf{u}_e}{\partial t} + (\mathbf{u}_e \cdot \nabla) \mathbf{u}_e \right) \quad (13)$$

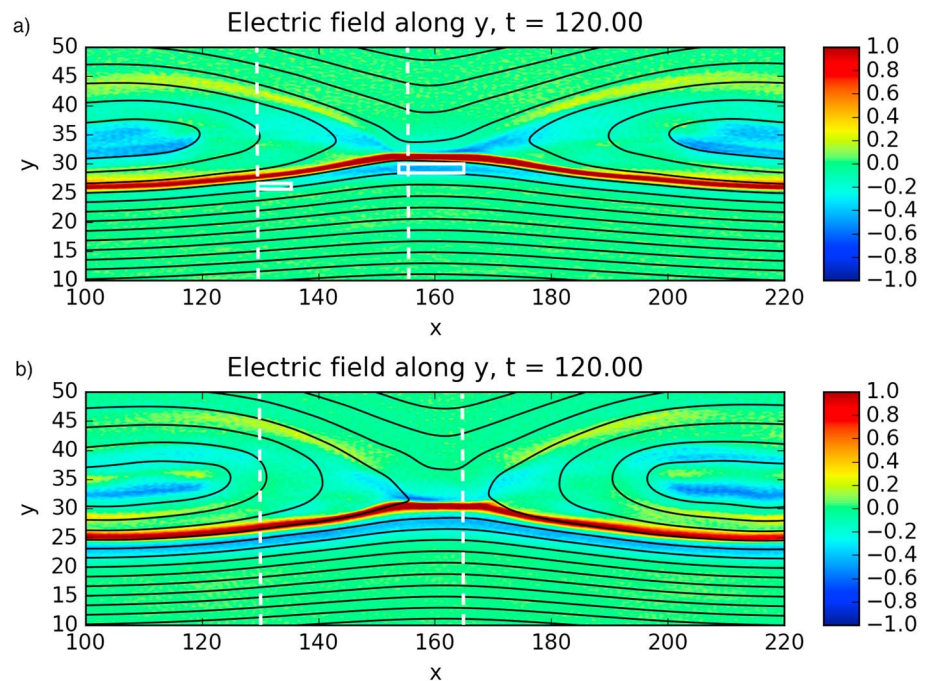


Figure 3. Normal electric field E_y in the box for (a) run A without cold ions and for (b) run B with cold ions. The white box at $x \in [155., 165.]$ and $y \in [27., 29.]$ indicates where particles are picked to form the particle distribution functions of Figures 5 and 6. The white box at $x \in [130., 135.]$ and $y \in [25.5, 26.5]$ indicates where particles are picked to form the particle distribution functions of Figure 9. The white vertical dashed lines indicate respectively $x = 130$ and the x location of the X line in both runs. Both pictures are obtained after averaging 20 time steps between $t = 119$ and $120\omega_{ci}^{-1}$ and smoothing the 2-D result with a Gaussian filter of $\sigma = 0.25$ in the x direction and $\sigma = 0.125$ in the y direction.

Figure 3 shows the electric field along y direction for both simulations without ((a) run A) and with ((b) run B) cold ions. In this section, we will focus on what happens near the X line, whose x location is given in Figure 3 by a vertical white dashed line. Another one gives the position $x = 130\delta_i$, which is the location of section 4 study.

3.1. Kinetic Dynamics Without Cold Ions

Let us first look at the simulation without cold ions (run A). In Figure 3a, we can see the normal electric field E_y for run A. The X point is located at $(x, y) \sim (160, 32)\delta_i$, the locus of the initial perturbation. The magnetosheath is located at $y > 32\delta_i$, and the magnetosphere at $y < 32\delta_i$. We can see in red the Hall electric field all along the magnetospheric separatrix. On the magnetosphere side, we can also see in blue the Larmor electric field located only close to the X line and fading out with the distance away from it.

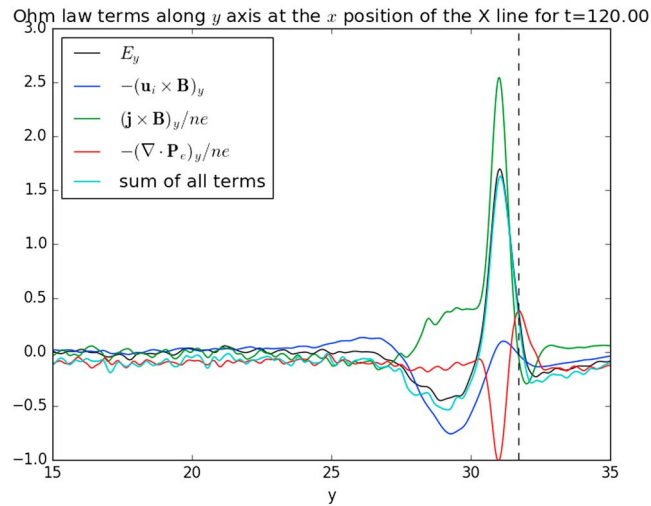


Figure 4. Different terms of the Ohm's law at the position of the X line in the x direction for run A. The vertical black dashed line gives the y position of the X line. The curve is obtained after averaging 20 times between $t = 119$ and $120\omega_{ci}^{-1}$ and smoothing the 2-D result with a Gaussian filter of $\sigma = 2.5$ in x direction and $\sigma = 0.125$ in y direction.

particle velocity distributions for all ions reduced to the v_y - v_z plane. The total ion distribution (Figure 5a) is composed of a quasi-isotropic population (the magnetosphere ions in Figure 5c, representing 77.16% of the box density) and a crescent-shaped distribution (the magnetosheath ions in Figure 5b, representing 22.84% of the box density). We note that magnetosheath ions have a clear positive out-of-plane velocity and magnetosphere ions have a comparatively small negative out-of-plane velocity. The shape of the magnetospheric ion distribution, slightly asymmetric in the v_z direction, can be interpreted as a diamagnetic drift of magnetosphere ions. The boundary layer is a location where the density of magnetosphere ions decreases, reaching zero far on the magnetosheath side. The magnetosheath ion distribution has a crescent shape which is similar to the electron distributions observed at the electron diffusion region [Hesse *et al.*, 2014; Burch *et al.*, 2016; Shay *et al.*, 2016]. This crescent shape distribution is explained by their bounce between the magnetospheric and magnetosheath magnetic field lines [Shay *et al.*, 2016; Phan *et al.*, 2016]. The only magnetosheath ions which are able to reach this area, on the magnetosphere side, are those doing their U-turn in this area or farther. Interestingly, most of the magnetosheath ions make their U-turn in the same region. This leads, from a fluid perspective, to a positive ion velocity in the out-of-plane direction at the sub-Larmor radius scale. Despite representing only 23% of the total density there, their large positive velocity has a strong contribution to the total ion bulk velocity, making it overall positive. In this region of positive B_x , the positive out-of-plane total ion bulk velocity is associated with a negative $\mathbf{u}_i \times \mathbf{B}$ term in the normal direction. This term, the only one locally negative (see Figure 4), explains the negative electric field. It is important here to note that although this electric field is supported by the ideal term, it is entirely resulting from a kinetic ion effect and therefore would not appear in fluid models.

To better illustrate the kinetic behavior of ions in the Larmor electric field area, we take a typical ion from the magnetosheath ion distribution (Figure 5b) and use it to initialize a test particle tracing. Using the electromagnetic configuration at $t = 120\omega_{ci}^{-1}$ with a steady state assumption, we look at the particle trajectory during $10\omega_{ci}^{-1}$. We choose the particle such that it does not have too much velocity in the x direction, which enables us to sample the bounce motion correctly with only one particle. The trajectory of this particle is represented in Figure 6. The in-plane trajectory in Figure 6a shows that the particle is bouncing between magnetic field lines of the magnetosheath (above the dashed line) and magnetosphere (below the dashed line). The out-of-plane trajectory in Figure 6c (projected on plane (y, z)) shows a drift of the particle in the z direction. This is a Speiser orbit drift, caused by the reversal of the magnetic field [Speiser, 1965]. We also observe a widening of the particle orbit, which means that the particle is gaining energy.

3.2. Kinetic Dynamics With Cold Ions

Let us now look at the simulation with cold ions. In Figure 3b, we can see the normal electric field E_y for run B. The first thing to be noticed is that the Larmor electric field is not confined around the X line anymore. This key

where e the proton charge, m_e the electron charge, \mathbf{u}_s is the fluid velocity of a species s (i for ions, e for electrons), and \vec{P}_e the electron pressure tensor. Figure 4 shows the main terms of the Ohm's law along the y direction. As shown by Malakit *et al.* [2013], we can see that the electric field at $y \approx 29$, i.e., the Larmor field signature, is mainly supported by the $-\mathbf{u}_i \times \mathbf{B}$ term. The magnetic field is positive on the magnetospheric side. So, for this term to be negative, we deduce that ions have a positive out-of-plane velocity. The origin of this out-of-plane velocity has now to be explained.

To understand the mechanism behind the Larmor electric field, we take all ions within $x = [155., 165.]\delta_i$ and $y = [27., 29.]\delta_i$ (right-hand side white box in Figure 3a) and plot in Figure 5 the

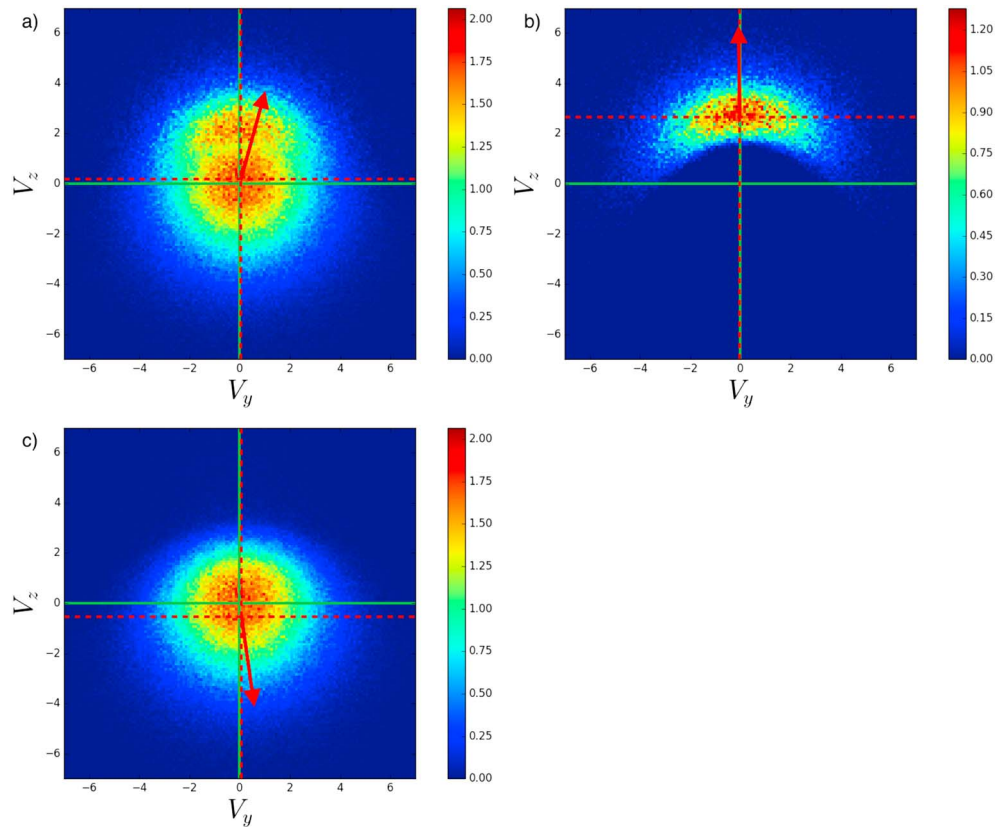


Figure 5. Ion distribution functions at the Larmor electric field location (see the right-hand side white box of Figure 3a). Distributions are shown for the normal versus out-of-plane velocities, i.e., the (v_y, v_z) space. They are calculated as the sum of the weight of each particle included into a $(\delta v_y, \delta v_z)$ box of velocity space, where $\delta v_y = \delta v_z = 0.1$. The thick green lines give the origin. The dashed red lines give the position of the mean velocity of the distribution. The red arrow shows the direction of the average velocity. (a) Total ion distribution. (b) Magnetosheath ion distribution. (c) Magnetosphere ion distribution. Magnetospheric and magnetosheath ions represent, respectively, 77.16% and 22.84% of the ion density in the box.

feature is further developed in section 4.2, where the region far from the X line is discussed in detail. If we focus on the X line region, however, the simulation shows very few differences with the case without cold ions. The Larmor electric field, associated with the unchanged magnetosheath ions, remains comparable.

In Figure 7, we show different quantities along a cut in the normal direction at the X point. In Figure 7a, densities for each ion species are shown. We can see there are still magnetosheath ions on the magnetospheric side and hot magnetospheric ions on the magnetosheath side, which is consistent with the results of section 3.1. In Figure 7b, we present the out-of-plane velocity for each ion population. As previously, we see that the out-of-plane velocity is positive for magnetosheath ions and negative for hot magnetospheric ions in the Larmor electric field area. However, contrary to hot magnetospheric ions, the cold magnetospheric ions there have a positive out-of-plane velocity. The reason for this difference is that cold ions are locally frozen in the magnetic field and experience an $\mathbf{E} \times \mathbf{B}$ drift. This is confirmed by Figure 7c, which shows the $-(\mathbf{u}_s \times \mathbf{B})_y$ components for each population. On this panel, the cold ion curve fits exactly the E_y curve within the Larmor electric field region, which means that they are frozen in. In contrast, the velocity of the other ion populations does not match this curve at all, meaning they are demagnetized.

To study the contribution of each population to Ohm's law terms, we can rewrite equation (13) as done by Toledo-Redondo *et al.* [2015]. We neglect here time variations and the contribution of electron inertia:

$$\mathbf{E} = -\frac{n_{ic}}{n} \mathbf{u}_{ic} \times \mathbf{B} - \frac{n_{ih}}{n} \mathbf{u}_{ih} \times \mathbf{B} - \frac{n_{ish}}{n} \mathbf{u}_{ish} \times \mathbf{B} + \frac{1}{en} \left(\mathbf{j} \times \mathbf{B} - \nabla \cdot \vec{P}_e \right) \quad (14)$$

Figure 7d shows the $-n_s/n(\mathbf{u}_s \times \mathbf{B})_y$ terms of the Ohm's law for each ion population. This plot shows that the main contributors to the Larmor electric field (i.e., the negative electric field between dotted lines) remain

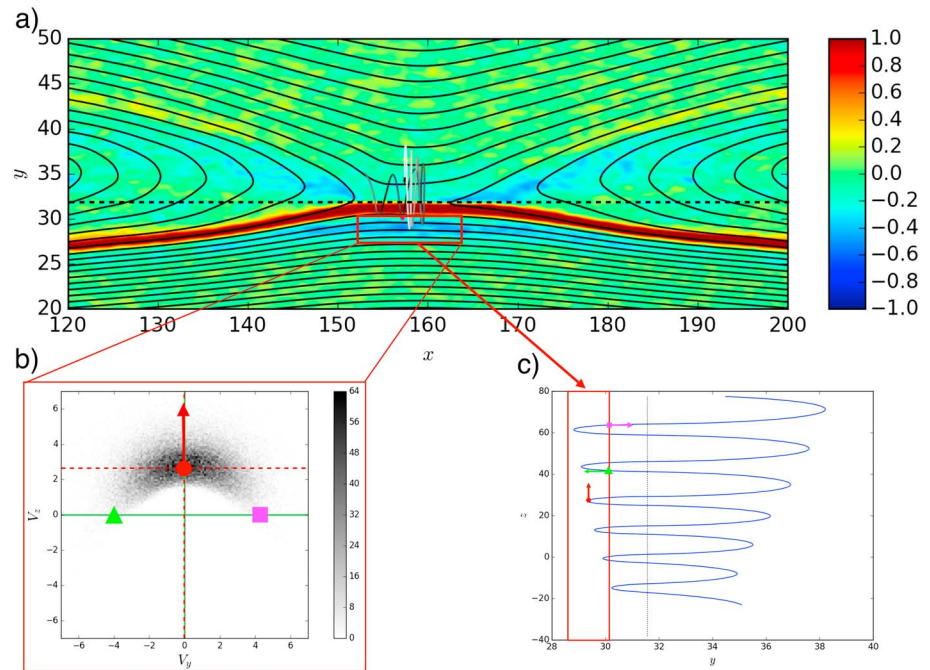


Figure 6. (a) Normal electric field E_y in the box with the in-plane trajectory of the test particle calculated in fixed electromagnetic fields. The color of the arrow depends on the kinetic energy of the particle: the lightest, the more energetic. In-plane magnetic field lines are depicted as thick black lines. The dashed line gives the y location of the X point. The red box represents the main area of Larmor electric field. (b) Particle distribution of magnetosheath ions located in the Larmor electric field (see Figure 5b). The colored points give the location in velocity space associated with the velocity arrows shown in Figure 6c. (c) Out-of-plane (y, z) trajectory of the test particle. The arrows symbolize the velocity of the test particle at a given position. Each of these velocities is associated with a point of the same color in Figure 6b.

the magnetosheath ions (blue line). However, we can also see a nonnegligible contribution from cold ions (red line). Because they drift in the Larmor electric field (they are magnetized there), they have a negative contribution to the electric field, which is contrary to the positive one from the demagnetized hot magnetospheric ions. In conclusion, close to the X line the Larmor electric field still exists and is associated with similar underlying dynamics of magnetosheath and hot magnetospheric ions. Cold ions are frozen and weakly contribute to the Larmor electric field.

4. Ion Kinetic Dynamics Far From the X Line

What initially makes the Larmor electric field feature interesting is its localization near the X line [Malakit et al., 2013]. However, we have seen on Figure 3b that for the simulation with cold ions, it is not located solely at the X line anymore. Far from the X line, the current sheet is broadened by the reconnection process, making it impossible for magnetosheath ions to bounce, as described in the previous section, and to create this Larmor electric field. Therefore, another mechanism, related to the presence of cold ions, has to take place to allow this field to exist there. In this section, we will look into more details at the differences between the cases with and without cold ions, and we will show why a negative electric field is seen below the magnetospheric separatrix in the presence of cold ions.

4.1. Kinetic Dynamics Without Cold Ions

Let us first consider the case without cold ions and look at the terms of the Ohm's law (equation (13)) far from the X line at $x = 130$. To simplify the analysis, we can ignore some terms that are negligible. The reconnection process being in a steady state, the $\partial \mathbf{u} / \partial t$ term is negligible. The inertial term $(\mathbf{u} \cdot \nabla) \mathbf{u}$ is also negligible except in the very vicinity of the X point [Hesse et al., 2014; Dargent et al., 2016].

The simplified Ohm's law can be written as follows:

$$\mathbf{E} = -\mathbf{u}_i \times \mathbf{B} + \frac{1}{en} \left(\mathbf{j} \times \mathbf{B} - \nabla \cdot \vec{P}_e \right) \quad (15)$$

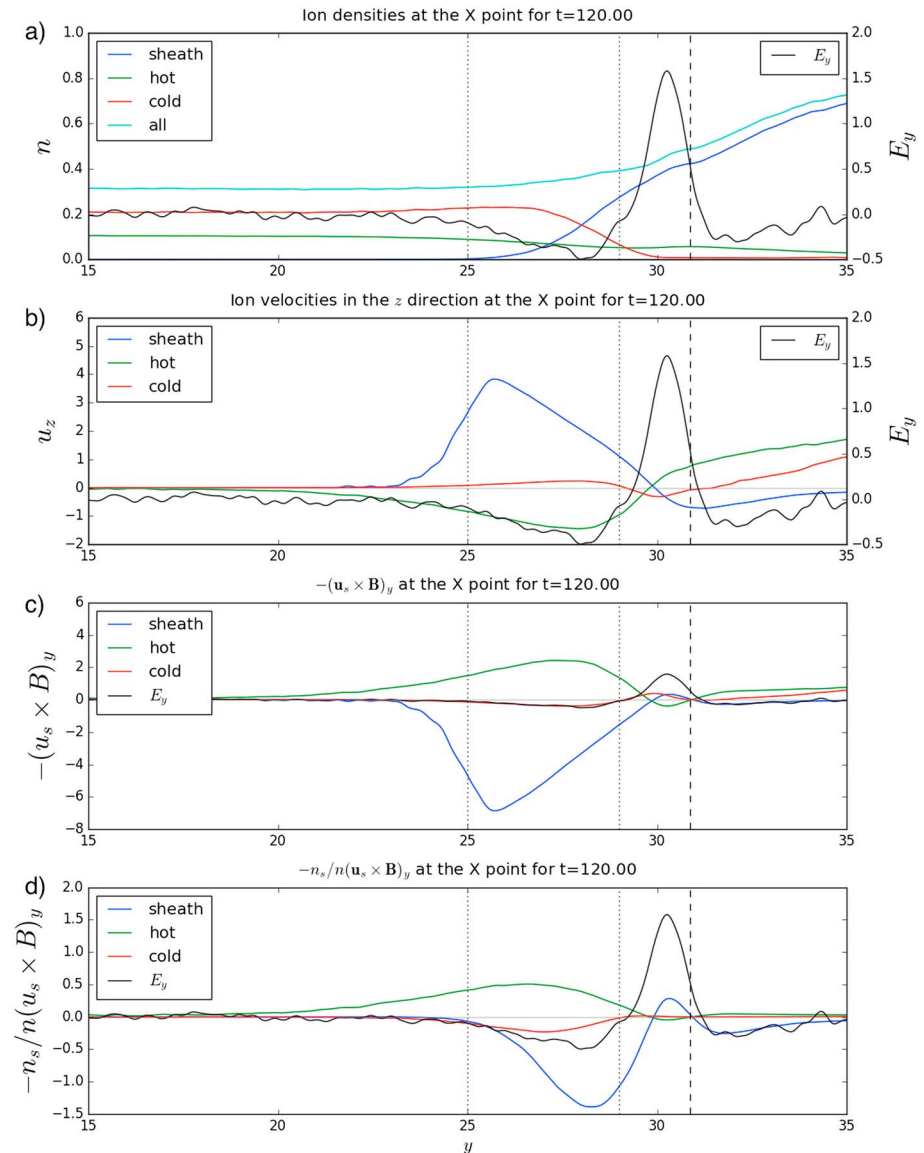


Figure 7. Different quantities for a cut at the position of the X line in the x direction in run B at $t = 120\omega_{ci}^{-1}$. The curves are obtained after smoothing with 2-D Gaussian filter of $\sigma = 1.5$ in x direction and $\sigma = 0.125$ in y direction. The normal electric field E_y is plotted in black on each panel. The vertical dashed line represents the X point position in y . The vertical dotted lines give arbitrary boundaries for the Larmor electric field. (a) Density of each ion species and total density. (b) Out-of-plane velocity of each ion species. (c) $-\mathbf{u}_s \times \mathbf{B}$ term of each ion species in the normal direction. (d) $-n_s/n_s \times \mathbf{B}$ term of each ion species in the normal direction.

Figure 8 presents these terms in a cut through the magnetopause along the normal direction y , together with the electric field E_y , away from the X line at $x = 130$. We first see that the pressure term $\nabla \cdot \vec{P}_e/ne$ is negligible everywhere. Then, one can notice that for $y \sim 25$ (i.e., the area next to the Hall electric field peak on the magnetospheric side) the $-\mathbf{u}_s \times \mathbf{B}$ term is positive and does not entirely balance the (negative) electric field, unlike the results at the X line in Figure 7. Even if the crescent shape of the magnetosheath ion distribution far from the X line (Figure 9b) looks like the distribution at the X line (Figure 5b), we observe that local magnetosheath ions are not bouncing in a Speiser fashion but are rather merely gyrating around magnetic field lines. Magnetosheath ions represent a smaller proportion of ions in the box (9.94% for Figure 9) compared to near the X line (22.84% for Figure 5), where the Speiser orbits (see Figure 6) allow more magnetosheath ions to reach the magnetosphere side. By contrast, the distribution of magnetosphere ions is qualitatively the same at $x = 130$ (Figure 9c) and at the X line (Figure 5c). The result is that the total out-of-plane velocity is negative

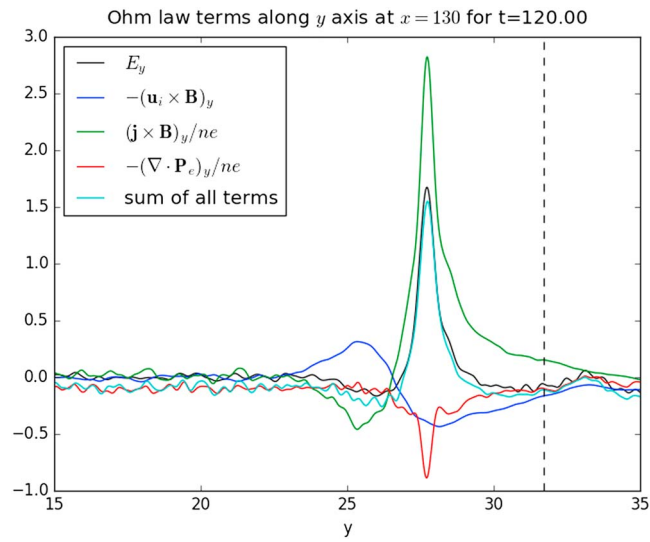


Figure 8. Different terms of the Ohm’s law at $x = 130\delta_i$ for run A. The vertical black dashed line gives the y position of the X line. The curve is obtained after averaging 20 times between $t = 119$ and $120\omega_{ci}^{-1}$ and smoothing the 2-D result with a Gaussian filter of $\sigma = 2.5$ in x direction and $\sigma = 0.125$ in y direction.

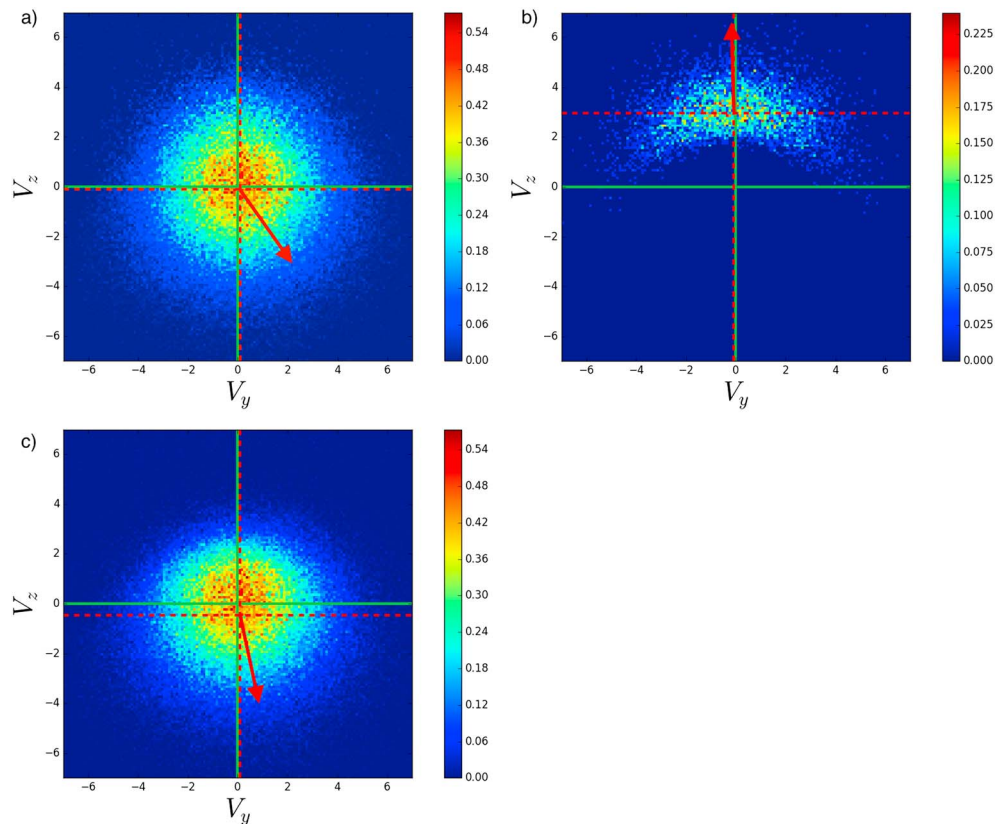


Figure 9. Ion particle distributions near the separatrix on the magnetosphere side of the boundary layer, and far from the X line. Particles are picked in a box for $x = [130., 135.]\delta_i$ and $y = [25.5, 26.5]\delta_i$. Distributions are shown for the normal versus out-of-plane velocities, i.e., the (v_y, v_z) plane. They are calculated as the sum of the weight of each particle included into a $(\delta v_y, \delta v_z)$ box of the velocity space, where $\delta v_y = \delta v_z = 0.1$. The thick green lines give the origin. The dashed red lines give the position of the distribution mean velocity. The red arrow shows the mean direction of the distribution velocity. (a) Total ion distribution. (b) Magnetosheath ion distribution. (c) Magnetosphere ion distribution. Magnetospheric and magnetosheath ions represent, respectively, 90.06% and 9.94% of the ion density in the box.

and that $\mathbf{u}_i \times \mathbf{B}$ has to be locally positive, contrary to what happens at the X line. The electric field below the separatrix at $y \approx 25$ is negative and much smaller than at the X line, as can also be seen in Figure 3a. This field gets smaller with distance from the X line. It is clear, from Figure 8, that the positive ion ideal term ($\mathbf{u}_i \times \mathbf{B}$) is mostly balanced by the Hall term ($\mathbf{j} \times \mathbf{B}$), i.e.,

$$(\mathbf{u}_i \times \mathbf{B})_y \approx \frac{1}{en} (\mathbf{j} \times \mathbf{B})_y \quad (16)$$

Equation (15) can also be rewritten for ions, neglecting the inertia term:

$$E_y = -(\mathbf{u}_i \times \mathbf{B})_y + \frac{1}{en} \left(\nabla \cdot \vec{P}_i \right)_y \quad (17)$$

Given $E_y \approx 0$ for $y \sim 25$, we have from equation (17)

$$(\mathbf{u}_i \times \mathbf{B})_y \approx \frac{1}{en} \left(\nabla \cdot \vec{P}_i \right)_y \quad (18)$$

Note that this result is consistent with a diamagnetic drift.

In this region next to the separatrix on the magnetospheric side, the ideal ion electric field ($\mathbf{u}_i \times \mathbf{B}$) therefore approximately equals the ion pressure term. Equation (18) is a key result here, as we will show in the next section that hot magnetospheric and magnetosheath ions essentially have the same behavior, the only difference in equation (17) being the contribution of the cold ions.

4.2. Kinetic Dynamics With Cold Ions

We now look at the same location in run B, in the presence of cold magnetospheric ions. In Figure 10, we can see the same quantities as in Figure 7, again for $x = 130\delta_i$ far from the X line. In Figure 10a, we can see that in the entire negative electric field area (between dotted lines), cold magnetospheric ions represent more than two thirds of the total density. Regarding magnetosheath ions, they are almost absent in that area, as already said for run A in the previous subsection. Figure 10b shows the same features as Figure 7b: magnetosheath ions have a positive out-of-plane velocity and hot magnetospheric ions a negative out-of-plane velocity. Cold magnetospheric ions, however, now contribute with a small positive out-of-plane velocity. The explanation for the cold ion velocity is the same as before. As shown in Figure 10c, cold ions are frozen into the magnetic field and $\mathbf{E} \times \mathbf{B}$ drift within it, while the other ion populations are locally demagnetized.

The ion momentum equation can be written as follows:

$$E_y = -\frac{n_d}{n} (\mathbf{u}_d \times \mathbf{B})_y - \frac{n_{ic}}{n} (\mathbf{u}_{ic} \times \mathbf{B})_y + \frac{1}{en} \left(\nabla \cdot \vec{P}_i \right)_y \quad (19)$$

where the subscript d refers to the demagnetized magnetosphere and magnetosheath ions ($d = ish + ih$). As shown in the Appendix A, the contribution of the cold ions to the pressure term is negligible, which allows to write the following:

$$\left(\nabla \cdot \vec{P}_i \right)_y = \left(\nabla \cdot \vec{P}_d \right)_y \quad (20)$$

Figure 10d shows the relative contribution of each population to the normal electric field. Comparing Figures 8 and 10d, we can see the Hall term does not contribute as much to the positive peak electric field (Hall electric field) at $y \sim 26$. This is consistent with spacecraft observations at the subsolar magnetopause [Toledo-Redondo *et al.*, 2015] and can be interpreted as a reduction of the Hall effect in presence of cold ions because those are coupled to the electrons and the magnetic field. In a second time, we notice that the cold ion contribution matches quite well the electric field in the negative electric field area (i.e., between dotted lines). On the other hand, the contribution of demagnetized ions (magnetosheath and hot magnetospheric ions together, light blue curve) is qualitatively the same as the $-\mathbf{u}_i \times \mathbf{B}$ contribution in Figure 8. Equation (16) is verified, but for demagnetized ions only: the Hall term (purple curve in Figure 10d) balances the demagnetized ions

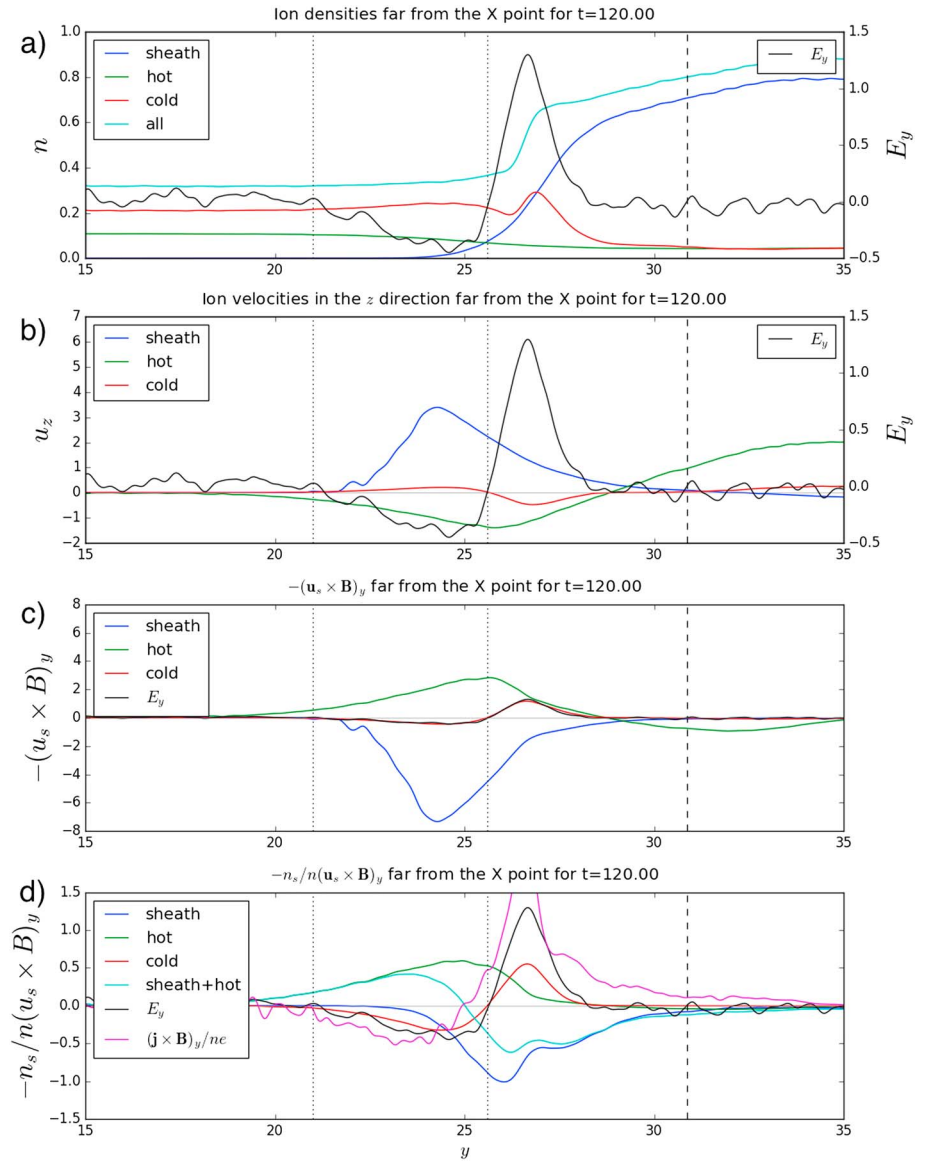


Figure 10. Different quantities for a cut far from the X line ($x = 130\delta_i$) in run B at $t = 120\omega_{ci}^{-1}$. The curves a obtained after smoothing data with 2-D Gaussian filter of $\sigma = 1.5$ in x direction and $\sigma = 0.125$ in y direction. The normal electric field E_y is plotted in black on each panel. The vertical dashed line represents the X point position in y . The vertical dotted lines give arbitrary boundaries for the negative electric field region. (a) Density of each ion species and total density. (b) Out-of-plane velocity of each ion species. (c) $-\mathbf{u}_s \times \mathbf{B}$ term of each ion species in the normal direction. (d) $-n_s/n(\mathbf{u}_s \times \mathbf{B})_y$ term of each ion species in the normal direction and for hot magnetospheric ions and magnetosheath ions together. The Hall term is added in purple.

contribution (light blue curve). Then, as in section 4.1, equation (18) is also verified. Equation (19) can then be split into two equations:

$$E_y \approx -\frac{n_{ic}}{n}(\mathbf{u}_{ic} \times \mathbf{B})_y \quad (21)$$

$$\frac{n_d}{n}(\mathbf{u}_d \times \mathbf{B})_y \approx \frac{1}{en} \left(\nabla \cdot \vec{P}_d \right)_y \quad (22)$$

Equation (21) shows that the electric field is associated with the drifting of the cold ions in the electric field, as demonstrated by the black and red curves in Figure 10d. Equation (22) then merely follows from the combination of equations (19), (20), and (21). When multiplied by n/n_d , it becomes identical to equation (18), but

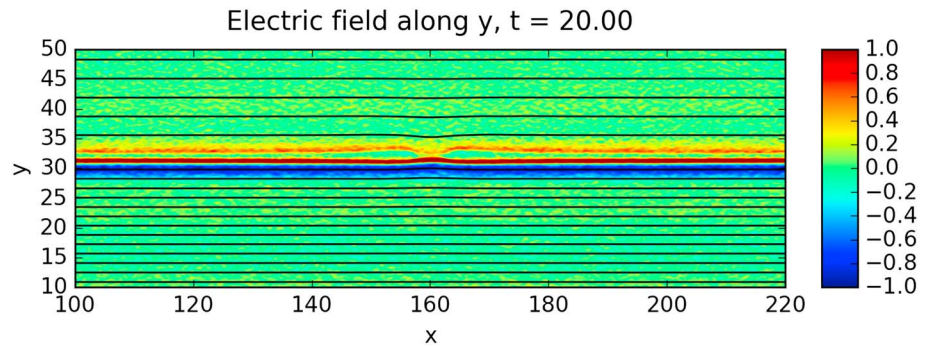


Figure 11. Normal electric field E_y in the box for the run A without cold ions for early time. The picture is obtained after averaging three files for times between $t = 19$ and $20\omega_{ci}^{-1}$ and smoothing the 2-D result with a Gaussian filter.

for demagnetized ions only. The fact that cold ions $\mathbf{E} \times \mathbf{B}$ drift here does not, however, explain why there is an electric field in the first place. To explain why we have an electric field there and not in run A, we looked at the beginning of the simulation. In both runs A and B, we notice we have initially an electric field everywhere along the layer (Figure 11 for $t = 20\omega_{ci}^{-1}$). Indeed, at the beginning, the boundary layer was thin everywhere. Therefore, magnetosheath ions were able to bounce (Speiser like) between the magnetosphere and magnetosheath magnetic field lines all along the current sheet. As explained in section 3.1, these ions produced a positive out-of-plane velocity and a negative electric field: the *Larmor electric field*. In run A without cold ions the bounce dynamics disappears everywhere but at the X line because reconnection broadens the current sheet everywhere but there. In other regions, the ions are demagnetized. Their kinetic dynamics leads to equation (18) from the fluid perspective. As a result the electric field vanishes everywhere except at the X line. In run B, hot magnetospheric and magnetosheath ions behave similarly; i.e., they satisfy equation (18). Cold ions, however, have a Larmor radius smaller than the width of the initial electric field structure and therefore drift within it. They contribute to the Ohm's law only through the ideal term and therefore maintain the electric field. This electric field has little effect on demagnetized magnetosheath and magnetospheric hot ions, whose Larmor radius is at much larger scale; hence, they behave as in run A. It is, however, interesting to notice that the strength of the electric field will strongly depend on the contribution of cold ions to the total density. Indeed, in Figure 10d the main contribution to the electric field comes from $-n_{ic}/n(\mathbf{u}_{ic} \times \mathbf{B})_y$, giving equation (21). However, cold ions are frozen in the field, which means

$$E_y = -(\mathbf{u}_{ic} \times \mathbf{B})_y \lesssim -\frac{n_{ic}}{n}(\mathbf{u}_{ic} \times \mathbf{B})_y \quad (23)$$

So to satisfy equations (21) and (23), we need $n_{ic}/n \approx 1$. Our results suggest that for an electric field to be maintained far from the X line, the density ratio between cold ions and magnetospheric ions needs to be sufficiently large. This condition allows to justify the approximation of $E_y \approx -n_{ic}/n(\mathbf{u}_{ic} \times \mathbf{B})$. In our case, cold ions represent about two thirds of the total density, which is enough to sustain the Larmor electric field. As this density ratio drops, we expect the electric field to decay.

5. Summary and Future Work

The magnetospheric plasma at the dayside magnetopause is a mix of different populations. In particular, low-energy species coming from the ionosphere can represent at times an important part of the total density and sometimes be largely dominant. Until now, the effect of cold ions on magnetic reconnection has been studied with observations only. In this paper, we have performed PIC simulations of asymmetric magnetic reconnection with and without cold ions on the magnetospheric side. Both initial conditions of the simulations share the same total density, total temperature, and electromagnetic fields. The only difference is the composition of the magnetospheric ion population. The run without cold ions has only one ion species on the magnetospheric side. The run with cold ions has two populations on magnetosphere side: a cold and a hot one, with a temperature ratio of 500. The presence of cold ions has been shown to drive an electric field along the magnetospheric separatrix looking like the Larmor electric field [Malakit et al., 2013], located at the magnetic reconnection X line.

We first investigated the mechanisms underlying this Larmor electric field. It corresponds to an electric field normal to the magnetopause, located near the X line on the magnetospheric side of the magnetopause.

We looked at magnetosphere and magnetosheath ions independently in the simulation without cold ions. Using test particle and particle distribution diagnostics, we showed that the origin of this electric field is purely kinetic. It is due to the bounce of the dense magnetosheath ions on the magnetospheric side in the area of magnetic field reversal. Their U-turn appears as a mean out-of-plane ion velocity, which, coupled with a stronger magnetic field on the magnetospheric side, is associated with an electric field. This phenomenon is the consequence of having a thin boundary layer between asymmetric plasmas with a magnetic field reversal. The local and steep magnetic field reversal leads to particle motions with Speiser-like orbits, and so that particles can reach far out on the other side of the boundary. The asymmetry leads the denser species most likely to create a mean velocity on the other side of the boundary (with a crescent shape distribution). At the magnetic reconnection site, both these conditions are met, which makes it a perfect location for a Larmor electric field to appear.

We analyzed the run with cold ions and demonstrated that there exists in this case an electric field signature akin to the Larmor electric field, but this one is present all along the separatrix and not just near the X line. We showed that cold ions are responsible for the existence of this elongated electric field signature. Due to their low temperature, these ions are frozen in the electric field; they $\mathbf{E} \times \mathbf{B}$ drift. Furthermore, at the beginning of the simulation, the current layer is thin everywhere, so a Larmor electric field appears everywhere along the separatrix on the magnetospheric side in both runs. Cold ions $\mathbf{E} \times \mathbf{B}$ drift into this initial Larmor electric field. This $\mathbf{E} \times \mathbf{B}$ drift velocity consistently supports the electric field within which they drift. Thanks to their dominant contribution to the density, they are, therefore, able to maintain this electric field once the layer becomes too thick for the Larmor electric field to be produced by Speiser orbiting. The initial electric field observed in the simulations may exist at the magnetopause if the layer is thin enough so that the finite Larmor radius effect exists. If so, this signature of cold ions should be observable thanks to the Magnetospheric Multiscale spacecraft. Whether it happens often and over which distance is however beyond the scope of this paper. This electric field can also have another origin. We also observed in our simulations that the Hall effect is reduced in presence of cold ions, as suggested by *Toledo-Redondo et al.* [2015]. More generally, this results mean that cold ions can affect electric field structures below the scales of hot magnetospheric and magnetosheath ions.

In this work, we focused on the effect of having a magnetospheric plasma with two populations, a hot and a cold one, but keeping the same total fluid properties identical in our two runs. However, in observations, the presence of cold ions typically increases the density, especially in the case of a plasmaspheric plume. Future works shall look at the combined effects of density and temperature of cold ions on magnetic reconnection.

Appendix A

We here focus on the area between dotted lines in Figure 10, and we show that in this area, $\nabla \cdot \vec{P}_i = \nabla \cdot \vec{P}_d$ in the y direction. This demonstration is based on two assumptions, which have to be locally verified:

1. Inertia terms of the Ohm's law are negligible.

$$2. \left(\nabla \cdot \vec{P}_e \right)_y = 0$$

In our case, those two conditions are satisfied between dotted lines. Furthermore, frozen species drift in the fields with the same perpendicular velocity, so $\mathbf{u}_e \times \mathbf{B} = \mathbf{u}_{ic} \times \mathbf{B}$.

First, we deduce some relations from these assumptions. Given that $\mathbf{u}_i = (n_{ic}\mathbf{u}_{ic} + n_d\mathbf{u}_d)/n$ and $\mathbf{u}_e \times \mathbf{B} = \mathbf{u}_{ic} \times \mathbf{B}$, we obtain

$$\mathbf{j} \times \mathbf{B} = en(\mathbf{u}_i - \mathbf{u}_e) \times \mathbf{B} \quad (\text{A1})$$

$$= en_d(\mathbf{u}_d - \mathbf{u}_e) \times \mathbf{B} \quad (\text{A2})$$

Thanks to the two assumptions, we can locally simplify the Ohm's law as follows:

$$E_y = -(\mathbf{u}_i \times \mathbf{B})_y + \frac{1}{en} \left(\nabla \cdot \vec{P}_i \right)_y \quad (\text{A3})$$

and

$$E_y = -(\mathbf{u}_i \times \mathbf{B})_y + \frac{1}{en} (\mathbf{j} \times \mathbf{B})_y \quad (\text{A4})$$

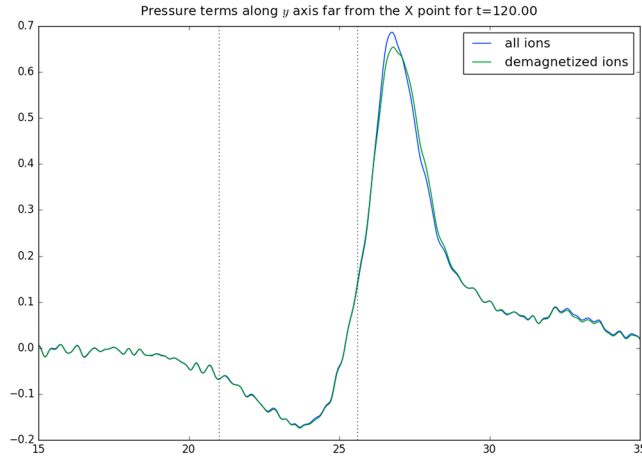


Figure A1. Pressure gradient at $x = 130\delta_i$ of all ions (blue curve) and demagnetized ions (i.e., hot magnetospheric and magnetosheath ions, green curve). The vertical dotted lines give arbitrary boundaries for the negative electric field region. The picture is obtained after averaging 20 files for times between $t = 119$ and $120\omega_{ci}^{-1}$ and smoothing the 2-D result with a Gaussian filter.

By identification, we obtain from equations (A3) and (A4)

$$(\mathbf{j} \times \mathbf{B})_y = \left(\nabla \cdot \vec{P}_i \right)_y \quad (\text{A5})$$

In a second time, we apply the fundamental principle of dynamics to every ion species:

$$nm_i \frac{d\mathbf{u}_i}{dt} = -\nabla \cdot \vec{P}_i + n(\mathbf{E} + \mathbf{u}_i \times \mathbf{B}) \quad (\text{A6})$$

$$n_d m_i \frac{d\mathbf{u}_d}{dt} = -\nabla \cdot \vec{P}_d + n_d(\mathbf{E} + \mathbf{u}_d \times \mathbf{B}) \quad (\text{A7})$$

$$n_{ic} m_i \frac{d\mathbf{u}_{ic}}{dt} = -\nabla \cdot \vec{P}_{ic} + n_{ic}(\mathbf{E} + \mathbf{u}_{ic} \times \mathbf{B}) \quad (\text{A8})$$

With a stationnarity assumption and neglecting steady inertia and along the y direction, we obtain the following:

$$0 = - \left(\nabla \cdot \vec{P}_i \right)_y + n (E_y + (\mathbf{u}_i \times \mathbf{B})_y) \quad (\text{A9})$$

$$0 = - \left(\nabla \cdot \vec{P}_d \right)_y + n_d (E_y + (\mathbf{u}_d \times \mathbf{B})_y) \quad (\text{A10})$$

$$0 = - \left(\nabla \cdot \vec{P}_{ic} \right)_y + n_{ic} (E_y + (\mathbf{u}_{ic} \times \mathbf{B})_y) \quad (\text{A11})$$

We deduce

$$\left(\nabla \cdot \vec{P}_d \right)_y = \frac{n_d}{n} \left(\nabla \cdot \vec{P}_i \right)_y - n_d ((\mathbf{u}_i - \mathbf{u}_d) \times \mathbf{B})_y \quad (\text{A12})$$

$$\left(\nabla \cdot \vec{P}_{ic} \right)_y = \frac{n_{ic}}{n} \left(\nabla \cdot \vec{P}_i \right)_y - n_{ic} ((\mathbf{u}_i - \mathbf{u}_{ic}) \times \mathbf{B})_y \quad (\text{A13})$$

Let's begin to work with equation (A13). We assumed that $\mathbf{u}_e = \mathbf{u}_{ic}$, so by using equation (A1), we have $\mathbf{u}_i - \mathbf{u}_{ic} = \mathbf{j}/n$. If we inject this into equation A13, we obtain thanks to equation (A5):

$$\left(\nabla \cdot \vec{P}_{ic} \right)_y = \frac{n_{ic}}{n} \left(\nabla \cdot \vec{P}_i \right)_y - \frac{n_{ic}}{n} (\mathbf{j} \times \mathbf{B})_y = 0 \quad (\text{A14})$$

In the same spirit, we inject equation (A2) into equation (A12) and we obtain the following:

$$\left(\nabla \cdot \vec{P}_d\right)_y = \frac{n_d}{n} \left(\nabla \cdot \vec{P}_i\right)_y - n_d((\mathbf{u}_i - \mathbf{u}_e) \times \mathbf{B})_y + (\mathbf{j} \times \mathbf{B})_y \quad (\text{A15})$$

$$= \frac{n_d}{n} \left(\nabla \cdot \vec{P}_i\right)_y - \frac{n_d}{n} (\mathbf{j} \times \mathbf{B})_y + (\mathbf{j} \times \mathbf{B})_y \quad (\text{A16})$$

$$= (\mathbf{j} \times \mathbf{B})_y \quad (\text{A17})$$

$$= \left(\nabla \cdot \vec{P}_i\right)_y \quad (\text{A18})$$

We have shown with those calculations that as long as the initial assumptions are verified, the pressure gradient of demagnetized ions is equal to the one of all ions. This result is confirmed by the simulation, as we can see in Figure A1, where both gradients are equal in the region of interest (between dotted lines). This means that the pressure gradient of a frozen ion population has to be negligible in front of the one of demagnetized ions.

Acknowledgments

The authors acknowledge the ANR for funding the project MON-ANR (ANR-13-PDOC-0027) supporting this research. The authors thank the SMILEI development team and especially Frederic Perez for the time he took to help us. This work was granted access to the HPC resources of IDRIS under the allocation i2015047231. We would like to thank Marie Flé for helping us in compiling the code on IDRIS machines. All data are available on request from the corresponding author. The work at the IRAP was supported by the CNRS and the CNES.

References

- André, M., and C. M. Cully (2012), Low-energy ions: A previously hidden solar system particle population, *Geophys. Res. Lett.*, *39*, L03101, doi:10.1029/2011GL050242.
- André, M., A. Vaivads, Y. V. Khotyaintsev, T. Laitinen, H. Nilsson, G. Stenberg, A. Fazakerley, and J. G. Trotignon (2010), Magnetic reconnection and cold plasma at the magnetopause, *Geophys. Res. Lett.*, *37*, L22108, doi:10.1029/2010GL044611.
- Baumjohann, W., and R. Treumann (1997), *Basic Space Plasma Physics*, Imperial Coll. Press, London.
- Borovsky, J. E., and M. H. Denton (2006), Effect of plasmaspheric drainage plumes on solar-wind/magnetosphere coupling, *Geophys. Res. Lett.*, *33*, L20101, doi:10.1029/2006GL026519.
- Borovsky, J. E., and M. Hesse (2007), The reconnection of magnetic fields between plasmas with different densities: Scaling relations, *Phys. Plasmas*, *14*(10), 102309, doi:10.1063/1.2772619.
- Borovsky, J. E., M. Hesse, J. Birn, and M. M. Kuznetsova (2008), What determines the reconnection rate at the dayside magnetosphere?, *J. Geophys. Res.*, *113*, A07210, doi:10.1029/2007JA012645.
- Burch, J. L., et al. (2016), Electron-scale measurements of magnetic reconnection in space, *Science*, *356*(6337), aaf2939, doi:10.1126/science.aaf2939.
- Cassak, P. A., and M. A. Shay (2007), Scaling of asymmetric magnetic reconnection: General theory and collisional simulations, *Phys. Plasmas*, *14*(10), 102114, doi:10.1063/1.2795630.
- Dargent, J., N. Aunai, G. Belmont, N. Dorville, B. Lavraud, and M. Hesse (2016), Full particle-in-cell simulations of kinetic equilibria and the role of the initial current sheet on steady asymmetric magnetic reconnection, *J. Plasma Phys.*, *82*(3), 905820305, doi:10.1017/S002237781600057X.
- De Keyser, J., M. Dunlop, C. Owen, B. Sonnerup, S. Haaland, A. Vaivads, G. Paschmann, R. Lundin, and L. Rezeau (2005), Magnetopause and boundary layer, *Space Sci. Rev.*, *118*(1–4), 231–320, doi:10.1007/s11214-005-3834-1.
- Drake, J. F., M. Swisdak, K. M. Schoeffler, B. N. Rogers, and S. Kobayashi (2006), Formation of secondary islands during magnetic reconnection, *Geophys. Res. Lett.*, *33*, L13105, doi:10.1029/2006GL025957.
- Fuselier, S. A., et al. (2016), Magnetospheric ion influence on magnetic reconnection at the duskside magnetopause, *Geophys. Res. Lett.*, *43*, 1435–1442, doi:10.1002/2015GL067358.
- Hesse, M., N. Aunai, D. Sibeck, and J. Birn (2014), On the electron diffusion region in planar, asymmetric, systems, *Geophys. Res. Lett.*, *41*, 8673–8680, doi:10.1002/2014GL061586.
- Lee, S. H., H. Zhang, Q.-G. Zong, A. Otto, D. G. Sibeck, Y. Wang, K.-H. Glassmeier, P. W. Daly, and H. Rème (2014), Plasma and energetic particle behaviors during asymmetric magnetic reconnection at the magnetopause, *J. Geophys. Res. Space Physics*, *119*, 1658–1672, doi:10.1002/2013JA019168.
- Malakit, K., M. A. Shay, P. A. Cassak, and D. Ruffolo (2013), New electric field in asymmetric magnetic reconnection, *Phys. Rev. Lett.*, *111*, 135001, doi:10.1103/PhysRevLett.111.135001.
- Matsui, H., T. Mukai, S. Ohtani, K. Hayashi, R. C. Elphic, M. F. Thomsen, and H. Matsumoto (1999), Cold dense plasma in the outer magnetosphere, *J. Geophys. Res.*, *104*(A11), 25,077–25,095, doi:10.1029/1999JA900046.
- Mozer, F. S., P. L. Pritchett, J. Bonnell, D. Sundkvist, and M. T. Chang (2008), Observations and simulations of asymmetric magnetic field reconnection, *J. Geophys. Res.*, *113*, A00C03, doi:10.1029/2008JA013535.
- Phan, T. D., et al. (2016), Ion Larmor radius effects near a reconnection x line at the magnetopause: THEMIS observations and simulation comparison, *Geophys. Res. Lett.*, *43*, 8844–8852, doi:10.1002/2016GL070224.
- Pritchett, P. L. (2008), Collisionless magnetic reconnection in an asymmetric current sheet, *J. Geophys. Res.*, *113*, A06210, doi:10.1029/2007JA012930.
- Sauvaud, J.-A., et al. (2001), Intermittent thermal plasma acceleration linked to sporadic motions of the magnetopause, first Cluster results, *Ann. Geophys.*, *19*, 1523–1532, doi:10.5194/angeo-19-1523-2001.
- Shay, M. A., J. F. Drake, B. N. Rogers, and R. E. Denton (2001), Alfvénic collisionless magnetic reconnection and the Hall term, *J. Geophys. Res.*, *106*, 3759–3772, doi:10.1029/1999JA001007.
- Shay, M. A., T. D. Phan, C. C. Haggerty, M. Fujimoto, J. F. Drake, K. Malakit, P. A. Cassak, and M. Swisdak (2016), Kinetic signatures of the region surrounding the X line in asymmetric (magnetopause) reconnection, *Geophys. Res. Lett.*, *43*, 4145–4154, doi:10.1002/2016GL069034.
- Speiser, T. W. (1965), Particle trajectories in model current sheets: 1. Analytical solutions, *J. Geophys. Res.*, *70*, 4219–4226, doi:10.1029/JZ070i017p04219.

- Toledo-Redondo, S., A. Vaivads, M. André, and Y. V. Khotyaintsev (2015), Modification of the Hall physics in magnetic reconnection due to cold ions at the Earth's magnetopause, *Geophys. Res. Lett.*, *42*, 6146–6154, doi:10.1002/2015GL065129.
- Toledo-Redondo, S., et al. (2016a), Cold ion demagnetization near the X-line of magnetic reconnection, *Geophys. Res. Lett.*, *43*, 6759–6767, doi:10.1002/2016GL069877.
- Toledo-Redondo, S., M. André, A. Vaivads, Y. V. Khotyaintsev, B. Lavraud, D. B. Graham, A. Divin, and N. Aunai (2016b), Cold ion heating at the dayside magnetopause during magnetic reconnection, *Geophys. Res. Lett.*, *43*, 58–66, doi:10.1002/2015GL067187.
- Walsh, B. M., T. D. Phan, D. G. Sibeck, and V. M. Souza (2014), The plasmaspheric plume and magnetopause reconnection, *Geophys. Res. Lett.*, *41*, 223–228, doi:10.1002/2013GL058802.
- Wang, S., L. M. Kistler, C. G. Mouikis, and S. M. Petrinec (2015), Dependence of the dayside magnetopause reconnection rate on local conditions, *J. Geophys. Res. Space Physics*, *120*, 6386–6408, doi:10.1002/2015JA021524.